Materials Science and Engineering A 520 (2009) 134–146

Contents lists available at ScienceDirect

Materials Science and Engineering A

journal homepage: www.elsevier.com/locate/msea

Evolution of texture during equal channel angular extrusion of commercially pure aluminum: Experiments and simulations

Satyam Suwas[a], R. Arruffat Massion[b], L.S. Tóth[b,*], J.-J. Fundenberger[c], B. Beausir[b]

[a] Department of Materials Engineering, Indian Institute of Science, Bangalore 560012, India
[b] Laboratoire de Physique et Mécanique des Matériaux, Université Paul Verlaine de Metz, Ile du Saulcy, F-57045 Metz Cedex 01, France
[c] Laboratoire d'Etude des Textures et Applications aux Matériaux, Université Paul Verlaine de Metz, Ile du Saulcy, F-57045 Metz Cedex 01, France

ARTICLE INFO

Article history:
Received 16 October 2008
Received in revised form 6 May 2009
Accepted 13 May 2009

Keywords:
Crystallographic texture
Equal channel angular extrusion
Aluminum
Non-octahedral slip

ABSTRACT

The evolution of crystallographic texture has been comprehensively studied for commercially pure Al as a function of amount of ECAE deformation for the three major routes of ECAE processing. It has been observed that processing through different routes leads to different type of texture, in both qualitative as well as quantitative sense. The results have been analyzed on the basis of existing concepts on ECAE deformation and simulations have been carried out using the simple shear model of ECAE implemented into the Viscoplastic Self Consistent model of polycrystal plasticity. The simulations revealed that non-octahedral slip is needed to reproduce the experimental texture development.

1. Introduction

Texture evolution during equal channel angular extrusion (ECAE) has received attention because the process involves imparting very high plastic strains in order to refine the microstructure; however, such a deformation is also likely to develop strong deformation texture. The ECAE process involves pressing of a well-lubricated billet into one of the two die-channels having the same cross-section placed at an angle (Fig. 1). It is now well established that during extrusion, the material is deformed successively nearly by simple shear in a narrow zone at the crossing plane of the channels (the shear plane). In this way, the complete billet (except small end regions) is deformed in the same uniform manner. As the overall billet geometry remains nearly constant during ECAE processing, multiple passes through the die are possible without any reduction in cross-sectional area.

ECAE is a discontinuous process, involving re-insertion of the sample in the die. The ECAE processing route can involve any number of passes through the die, by either clockwise (CW) or counter clockwise (CCW) rotations, usually about the sample's longitudinal (or bar) axis, between subsequent ECAE passes: A, no bar axis rotation; C, 180° rotation after every pass; Ba, clockwise 90° rotation after even numbered passes and counter clockwise 90° after odd numbered passes; and B_c, 90° rotation after every pass. All possible ECAE routes lead to changes in strain path, including the original route A that involves no intermediate rotation about the sample bar axis between passes.

The evolution of the deformed state, microstructure as well as texture, during deformation by ECAE, and the mechanisms that lead to grain refinement to the sub-micron scale, have been studied by several research groups in the recent past including the group of present authors [1–31]. A comprehensive review of texture development in ECAE is given by Beyerlin and Tóth [32]. However, the texture development in aluminum using ECAE does not lead to unique agreement in terms of effect of strain and strain path. There are many reasons for this. One of them is that the starting conditions of the material prior to ECAE are generally not uniquely reported in these investigations. It is well known that the starting texture has a very significant role on texture evolved after deformation. Moreover, most of the studies documented so far largely rely on pole figure measurements, in which different crystal orientations can overlap. More precise information on texture can be obtained with the help of three-dimensional texture analysis using orientation distribution function (ODF), which can be derived from pole figures.

The present study is realized using the ODF method for texture analysis of materials processed through the routes A, B_c and C of ECAE with identical starting material. The number of passes has been limited to five for each of the routes. The first pass is common for each route, so differences can be obtained starting from the second pass. Thus, considering the first pass deformed material

* Corresponding author. Tel.: +33 387547238; fax: +33 387315366.
E-mail address: toth@univ-metz.fr (L.S. Tóth).

0921-5093/$ – see front matter © 2009 Elsevier B.V. All rights reserved.
doi:10.1016/j.msea.2009.05.028

Table 1
Chemical composition of the starting material.

Element	Al	Si	Fe	Cu	Mn	Mg	Cr	Zn	Ti	V	Pb
Wt%	99.60	0.12	0.27	<0.005	<0.005	<0.005	<0.005	0.01	0.01	<0.005	<0.005

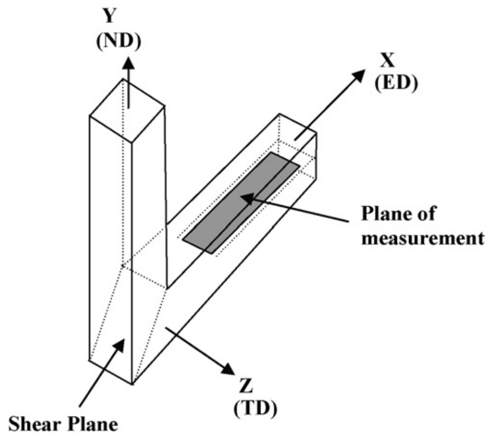

Fig. 1. Texture measurement plane (*XZ*) with reference to ECAE geometry.

as the initial (already deformed) state, four additional passes will bring the material into the initial sample configuration after having undergone through the routes B_c and C. This is why we carried out five passes for each route.

2. Material and methods

Commercially pure aluminum used for the present study was received in the form of rolled and annealed plate with 10 mm thickness. The chemical composition of the starting material is given in Table 1. Fig. 2 shows the microstructure of the starting material. It consists of quite flattened grains with an equivalent grain size of ~200 μm. Specimens with dimensions of 100 mm × 10 mm × 10 mm (rectangular cross-section) were machined from the rolled plates. The ECAE experiments were carried out at a cross head speed of 1 mm s^{-1} at room temperature using a Zwick 200 kN screw driven press and a die set with rectangular intersection of the extrusion channels (90°) without any rounding of the corner region. The samples were subjected to routes A, B_c and C.

2.1. Measurement and representation of texture

Texture measurements were carried out by X-ray diffraction using a Siemens D-5000 Texture Goniometer (Cu K_α radiation, λ = 1.5406 Å). For each sample (area 25 mm × 10 mm), the texture was examined through pole figures as well by calculating orientation distribution functions (ODF), which describe the crystallite orientation densities in a three-dimensional orientation space defined by the Euler angles ϕ_1, φ, ϕ_2. For this purpose, from each texture (1 1 1), (2 0 0) and (2 2 0) pole figures were recorded on the mid-horizontal plane (*XZ*) of the sample (Fig. 1), in the ND plane, using Schultz-reflection mode. This choice of the measuring plane was selected in order to avoid the texture gradient inherently present in an ECAE deformed sample [28–30]. Namely, in a rectangular channel, the texture gradient can be relevant in the ND direction. Thus, in a plane perpendicular to it the texture corresponds to the well defined middle position and the possibly existing variation along the ND axis does not affect the measured texture. The ODFs were calculated using the softwares developed at LETAM, University of Metz, and by Van Houtte [33], without imposing any restriction on symmetry, that is, assuming triclinic sample symmetry using the series expansion method of Bunge [34] with l_{max} = 22.

2.2. Microstructural investigation

The microstructural examination has been carried out using a JEOL 2000 Field Emission Gun Scanning Electron Microscope (FEG-SEM) with EBSD attachment. The results were analysed using the software “Channel 5” developed by HKL technology.

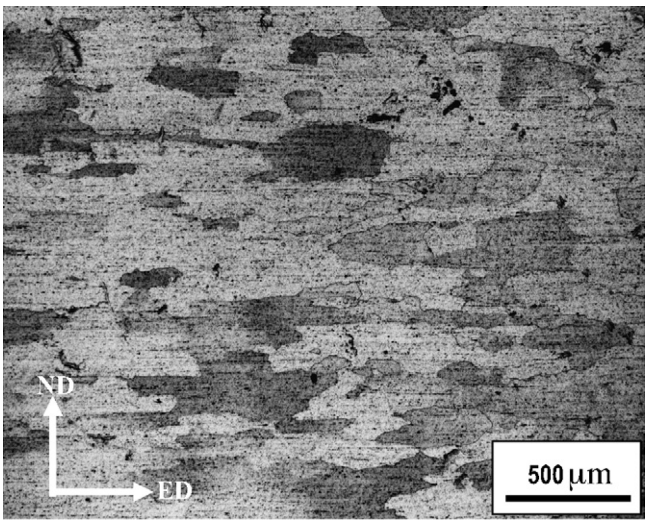

Fig. 2. Optical micrograph recorded on the *XY* plane of the material before ECAE.

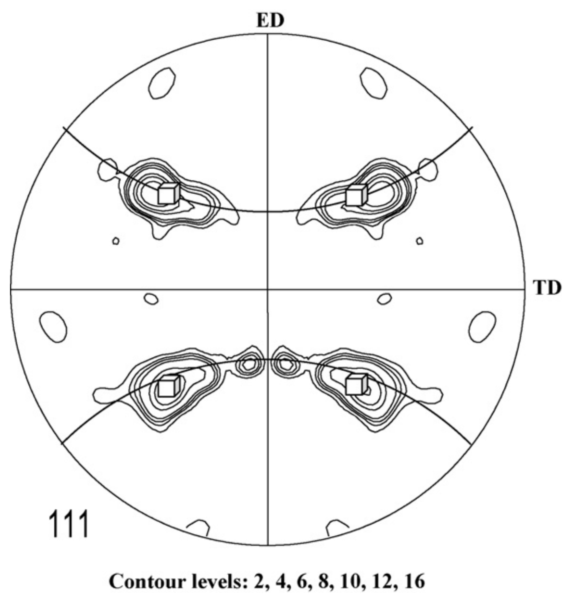

Fig. 3. (1 1 1) pole figure for the starting material. Cube symbol indicates the cube position.

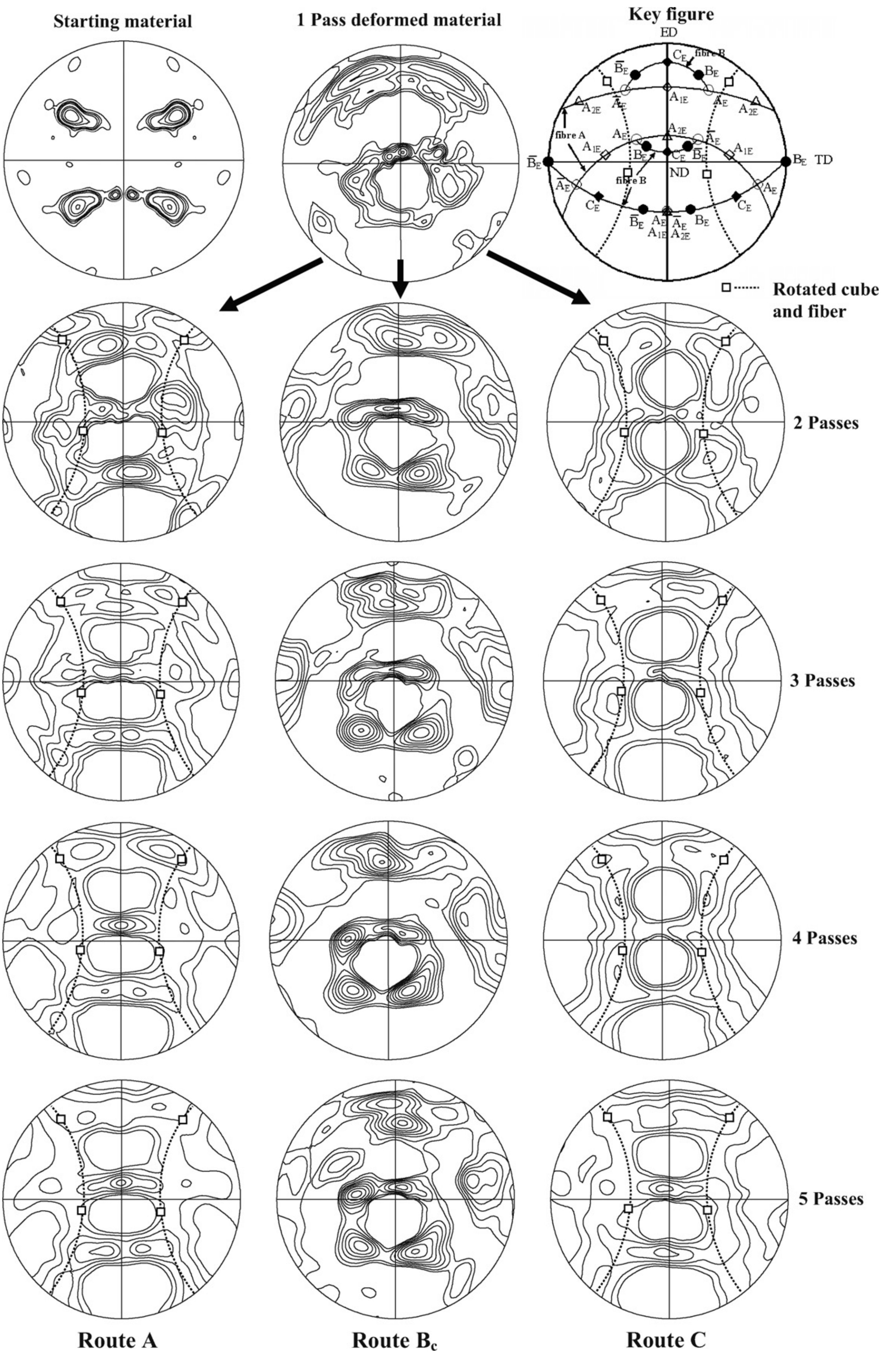

Fig. 4. (1 1 1) pole figure of the starting and the EACE deformed materials with a key figure showing different components and fibers of the ideal ECAE texture.

3. Experimental results and analysis

3.1. Crystallographic texture

The (1 1 1) pole figures for the starting material are shown in Fig. 3. The pole figure clearly indicates the presence of a very strong cube texture in the material. In addition to the most intense cube component, there is a partial fiber around the cube position with the ⟨1 0 0⟩ direction parallel to ED. The maximum pole density observed is 16 multiples of a random distribution.

Appreciable changes in the texture takes place, however, even after one ECAE pass. The experimental (1 1 1) pole figures for all the ECAE processed materials are also shown in Fig. 4 along with a key figure. As the ECAE deformation is near simple shear in the intersection plane of the two channels, the ideal ECAE texture components are the same as those known already for simple shear; they are just rotated by 45° with respect to the ECAE reference system, see a basic work about ideal orientations in a 90° ECAE in [13]. The main fibers in this rotated reference system are the A and B; they are defined by their Miller indices {1 1 1} and ⟨1 1 0⟩ parallel to the shear plane and shear direction, respectively. The shear plane is the intersection plane of the channels and the shear direction is within this plane, oriented towards the outer corner of the die (it is negative). The nomenclature of the texture components for ECAE is done according to our previous paper [13].

All the route A and route C pole figures appear symmetrical about the ND/ED plane, while there are noticeable deviations from this symmetry for route B_c. While for a given route, there are little differences in the texture with increasing the number of passes, the textures differ from one route to another. The common feature in all the pole figures is the occurrence of three peaks on the ND-ED line. The main difference appears in terms of splitting of the components at higher reductions, which in another way can be visualized in terms of shifting of the poles from ideal components along the B fiber. It should be noted, however, that the pole figures are unsymmetrical with respect to the transverse direction (TD), the maximum intensity poles being rotated by an angle around TD. This unsymmetrical arrangement is observed for all ECAE passes. The rotation angle of the pole figure around TD, however, does not seem to depend on the degree of straining. A remarkable observation from these pole figures is that characteristic texture develops in the second pass itself for each of the routes. It can be seen that

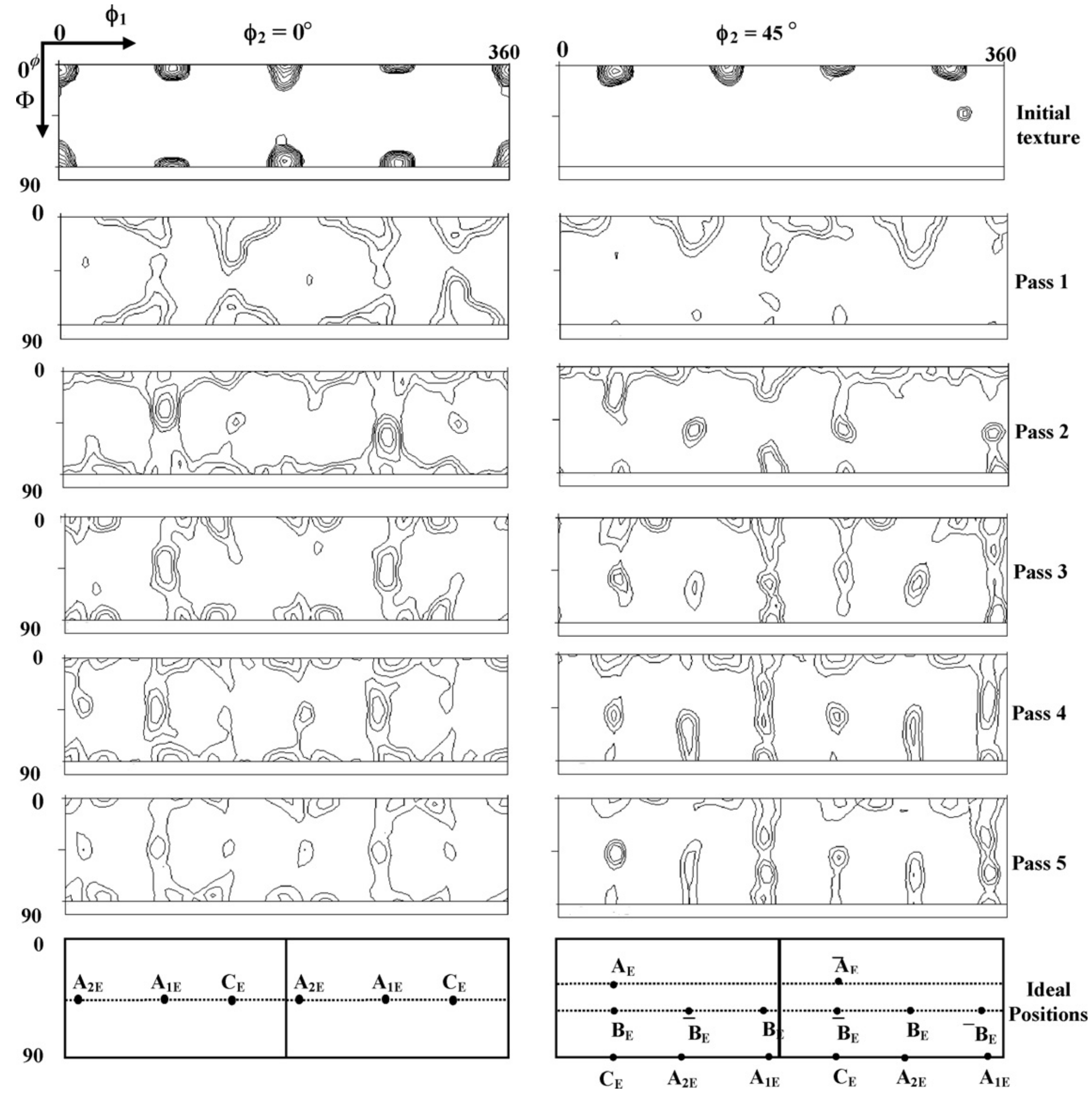

Fig. 5. $\phi_2 = 0°$ and $\phi_2 = 45°$ sections of the ODF for the ECAE samples before ECAE, processed to one pass and further through route A (2–5 passes) and a key figure showing components of ideal ECAE texture. Iso-levels in the initial texture: 10, 13, 16, 20, 25, 32, 40, 50. In all other textures, the following iso-levels were used: 2, 3, 4, 6, 8.

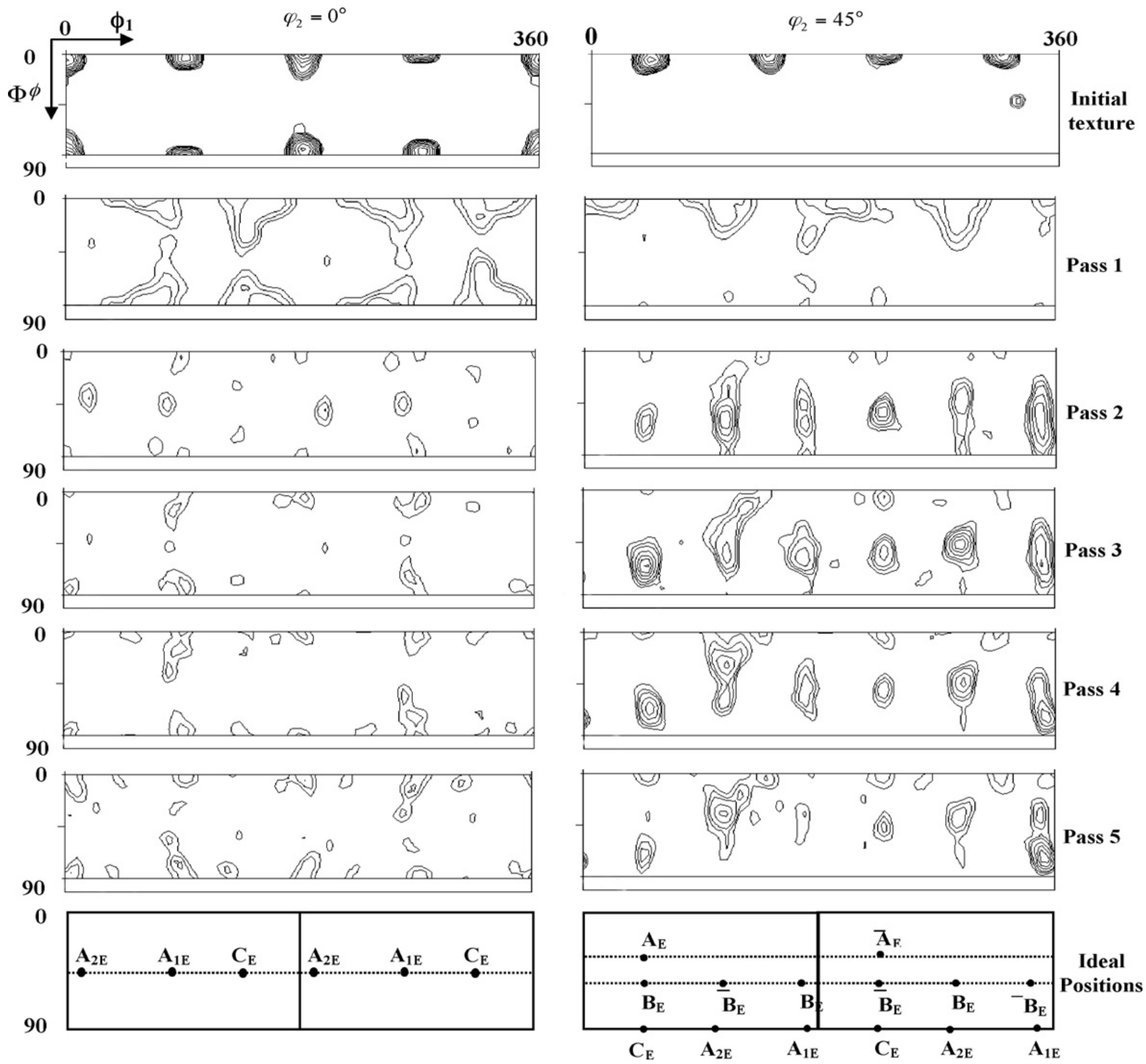

Fig. 6. $\phi_2 = 0°$ and $\phi_2 = 45°$ sections of the ODF for the ECAE samples before ECAE, processed to one pass and further through route B_c (2–5 passes) and a key figure showing components of ideal ECAE texture. Iso-levels in the initial texture: 10, 13, 16, 20, 25, 32, 40, 50. In all other textures, the following iso-levels were used: 2, 3, 4, 6, 8, 10, 12.

the textures of route A processed samples gradually weaken after the second pass, while the ones for route B_c strengthen. For route C materials, there is no clear trend.

In totality, the following main observation can be made out of the pole figures: the course of texture development is entirely different for the three routes of ECAE, and the sequence of texture development is quite systematic.

As mentioned before, ODFs describe textures better than pole figures. In the following, the texture results are presented in the form of orientation distribution functions for each of the measurements. For FCC materials, the sections $\phi_2 = 0°$ and $\phi_2 = 45°$ of the ODF space are usually used to present ODFs of shear textures as they contain the most important orientations. They will be employed also in the present work for the presentation of the experimental ODFs. For the simulated ODFs, mostly the $\phi_2 = 45°$ section will be used as it contains also all those ideal components that appear in the $\phi_2 = 0°$ section. This allows to shorten the ODF figures and to present more simulation results. The tendencies of the ODFs can be clearly seen in the single $\phi_2 = 45°$ section. Note that in all ODF sections, the range of the ϕ_1 Euler angle is from 0° to 360°, as the ODFs were calculated without imposing any sample symmetry.

The experimental ODFs obtained for the routes A, B_c and C are displayed in Figs. 5–7, respectively. One could expect a twofold symmetry in routes A and C, which can be quite well verified in the ODFs in all passes in Figs. 5 and 7. Such symmetry is due to the simple shear process of ECAE. Nevertheless, there are two reasons to have some deviations from the monoclinic symmetry: the first one is the deviations of the strain state from pure simple shear and the second one is the relatively large initial grain size. The latter concerns mostly the first pass as grain refinement by large plastic strain and dynamic recrystallization both lower the grain size in subsequent passes.

The route A processed material presents a very systematic texture evolution in the ODF plots of Fig. 5. In the first pass, the initially very strong cube texture disappears and the remnants of the cube related texture components are distributed along the ⟨0 0 1⟩|| TD fiber which will be called cube-fiber in the following. As the deformation proceeds, the intensities of components along this fiber decreases, however, they prevail up to the fifth (final) pass. It is clear that the A_{2E} and C_E components are vanishingly weak for all the cases, while the A_{1E} component is prominent in the texture. Concerning the A_E, $\bar{A}_E$ and B_E, $\bar{B}_E$ components, they are not seen after the first pass, then develop progressively with increasing pass number.

The ODF of materials processed through route B_c (Fig. 6) shows rather a strong texture and the course of texture development differs from route A. The texture of these materials is characterized

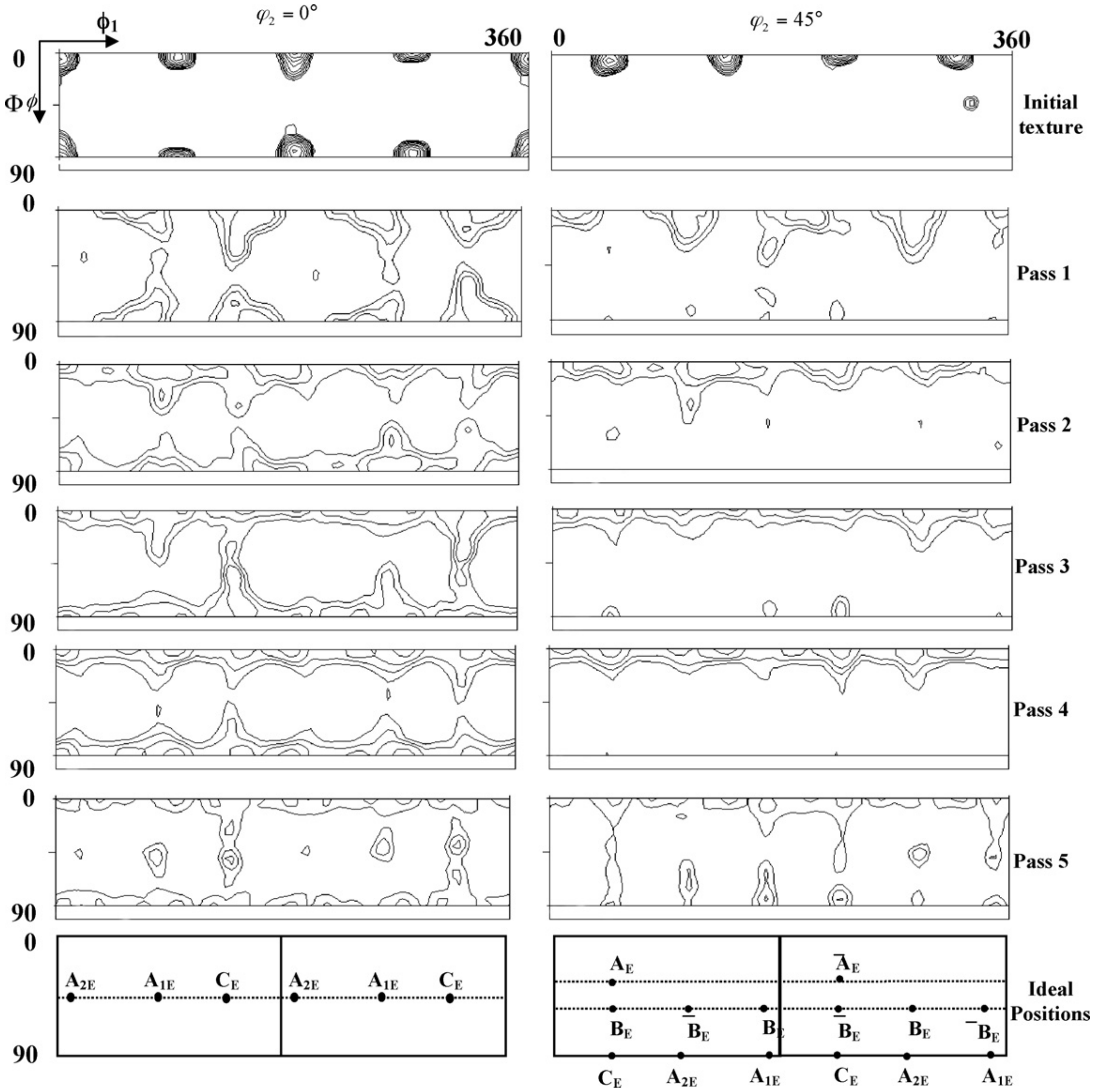

Fig. 7. $\phi_2 = 0°$ and $\phi_2 = 45°$ sections of the ODF for the ECAE samples before ECAE, processed to one pass and further through route C (2–5 passes) and a key figure showing components of ideal ECAE texture. Iso-levels in the initial texture: 10, 13, 16, 20, 25, 32, 40, 50. In all other textures, the following iso-levels were used: 2, 3, 4, 6.

by the presence of strong $B_E/\bar{B}_E$ components in all the passes. The third strong component that appears in these materials is at the location (ϕ_1, φ, ϕ_2 = 110°, 30°, 45°) corresponding to the component $\sim(5\bar{1}\bar{0}2)$ || ND plane and $\sim[\bar{5}\bar{2}3]$ || ED. This component is quite present in the ODF of all the route B_c processed samples, but becomes more prominent in the 4th and 5th pass deformed samples. It shows a systematic trend of evolution. In this paper, we name this component as B'_E. The other components, that belong to the so-called A fiber of shear textures; the A_E, $\bar{A}_E$ and A_{1E}, A_{2E}, remain always at low intensity. Concerning the evolution of the initial cube component, the ODF of these route B_c samples show isolated weak rotated cube components. They are generally weaker than in route A.

In the ODF of route C processed materials (Fig. 7), the rotated cube forms a continuous cube-fiber and remains quite strong after each pass. The stability of a rotated cube orientation is very high for this route. Although the A_{2E} component is not present in the ODF of any of the materials processed through this route, the C_E component appears in an oscillatory manner, that is, in the 1st, 3rd and 5th passes. In the fifth pass, a weak A_{1E} component also appears. The ODF of the fifth pass material through this route shows the tendency of acquisition of a texture that is observed in route A samples.

Fig. 8(a–g) shows the variation in volume fractions of A_{2E}, A_{1E} and C_E components, while Fig. 8(h) displays the value of $f(g)_{max}$ as a function of number of ECAE passes for different routes. The volume fractions were computed by integrating the ODF within a 15° distance in Euler space from the ideal component orientation. It might result in some limited overlapping of the volume fractions of neighboring components, nevertheless, the relative strengths of the components are well represented by this technique. The texture of route B_c material is to be noted on one extreme with predominant $B_E/\bar{B}_E/B'_E$ components, while the texture of route C materials is on the other extreme with a complete absence of these components. Texture of route A materials lies in between, with somewhat weaker B_E components.

3.2. Microstructural observations

Fig. 9 shows the EBSD generated micrographs for five passes of all the routes belonging to ECAE deformation. The micrographs

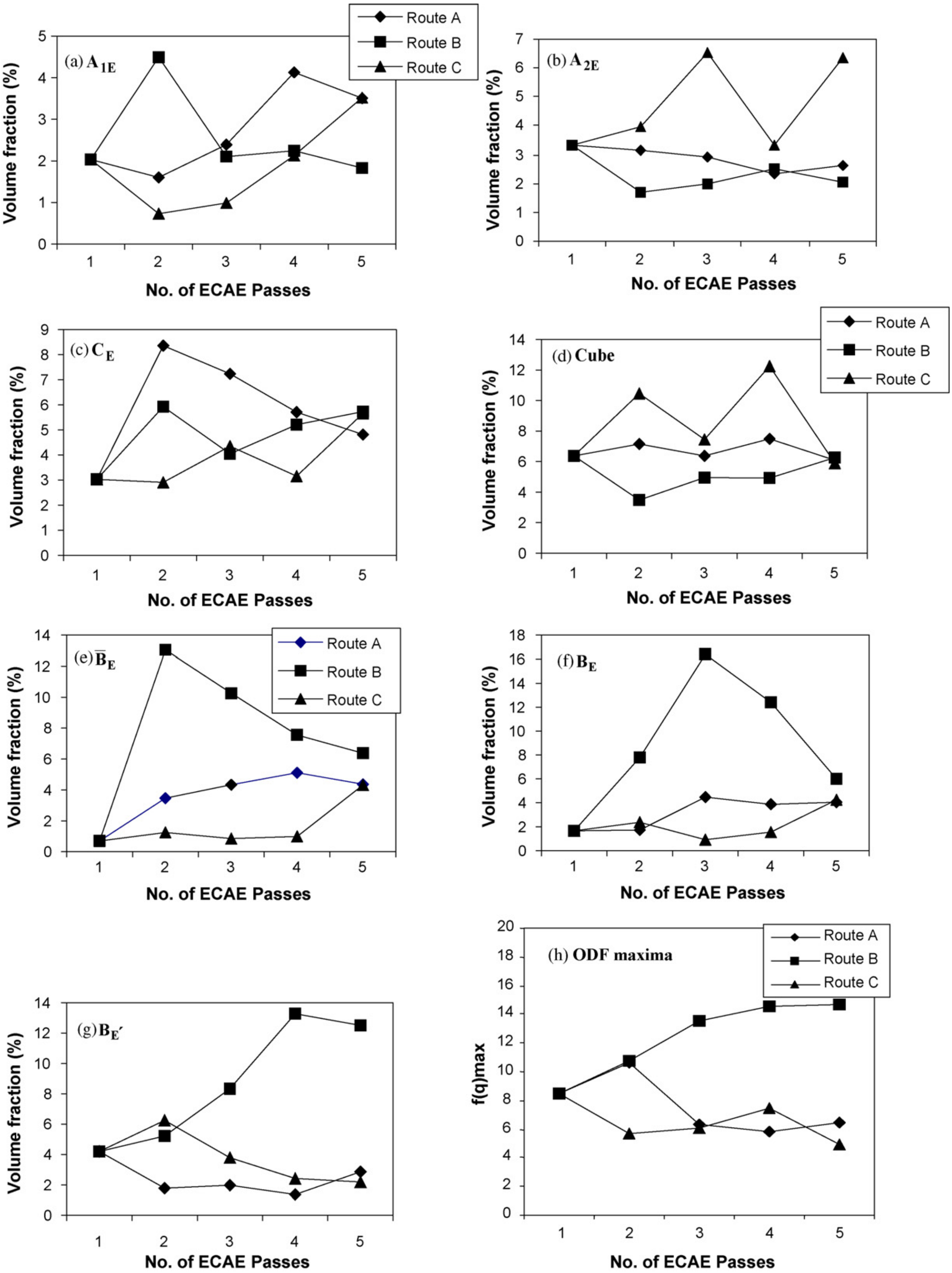

Fig. 8. Volume fractions for different texture components for each of the three processing routes A, B_c and C (a–g) and overall ODF maxima (h).

clearly depict the grain fragmentation. Fig. 10 shows the misorientation distribution for the two- and five-pass deformed materials. It can be seen that routes B_c and C develop relatively large fraction of misoriented grains compared to route A, the former having the highest degree of misorientation.

4. Texture simulation

Texture modeling was carried out considering the simple shear approach, originally proposed by Segal [1]. In this model, the deformation mode considered for the process is simple shear that takes

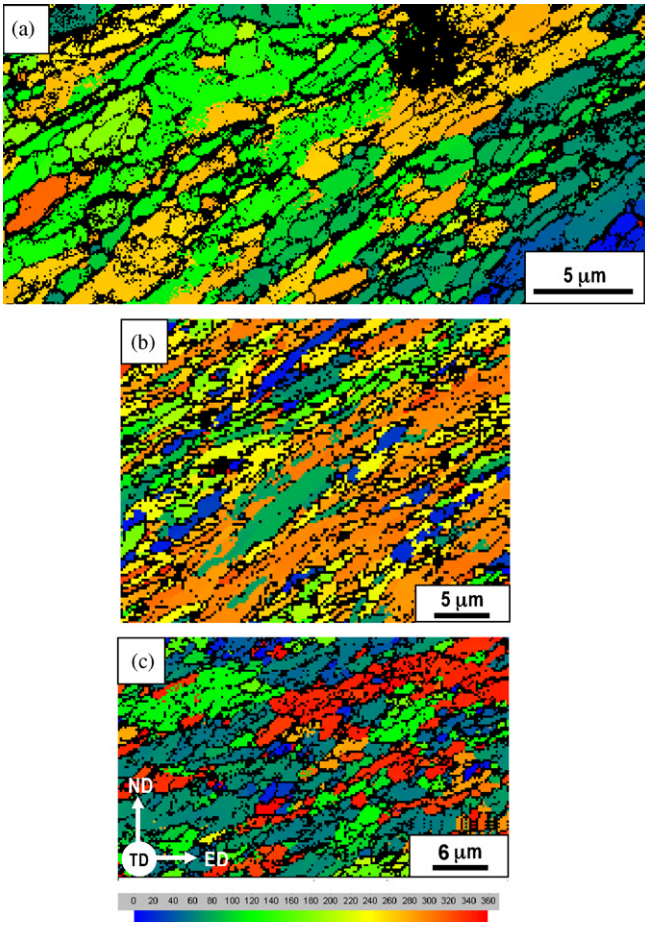

Fig. 9. Electron backscattered micrographs recorded on the *XY* plane of the material after ECAE: (a) route A after five passes, (b) route B_c after five passes and (c) route C after five passes.

place on the 45° intersection plane of the two channels. The more sophisticated flow line model proposed earlier [13] was also tested for the present experiments. It was found, however, that it is better for the higher values of flow line shape parameter (n), for which case the flow line model approaches the simple shear model. Therefore, only the simple shear model results are presented here.

Simulations have been carried out using the Viscoplastic Self Consistent (VPSC) model in its finite element tuned version [35]. The strain rate sensitivity index of crystallographic slip was chosen to be 0.05. The initial texture was discretized to 3000 grain orientations and was used in the first pass. In addition to the 12 $\{1\,1\,1\}\langle1\,1\,0\rangle$ fcc slip systems, the possibility of non-octahedral slip, that is the $\{1\,0\,0\}\langle1\,1\,0\rangle$ slip systems were also considered. This idea was inspired from the works of Bacroix, Driver and co-workers [36–44] who showed that non-octahedral slip is necessary for a successful simulation of the evolution of the texture in Al. When two families of slip systems are used, it is necessary to know their relative strengths. Bacroix and Jonas [36] showed that the maximum value of the relative crss $r_{\tau c}$, defined by the formula $r_{\tau c} = \tau_c\{1\,0\,0\}/\tau_c\{1\,1\,1\}$, is $\sqrt{3}$. According to our studies, there is no general lower limit because the $\{1\,0\,0\}$ slip alone cannot accommodate arbitrary deformation mode. Values between $r_{\tau c} = 0.8$ and $r_{\tau c} = 1.5$ were applied in [36]. As strain hardening is expected to equalize the strengths of the slip systems at large strains, a relatively high $r_{\tau c} = 1.5$ value was used in the first ECAE pass which was lowered to $r_{\tau c} = 1$ in all subsequent passes, for all routes. This technique is applied in order to account for strain hardening. Although during a single pass, the relative critical stresses of the slip systems were not changed, this approach takes into account strain hardening in a first order.

For modeling several ECAE passes, two schemes were applied in this work: the so-called 'simulation in continue' and 'simulation with texture updating' [13]. In the first technique, the grain output orientations of the previous pass were introduced as the input orientations of the next pass. In the texture updated technique, the experimentally measured output texture of the previous pass was discretized and introduced as the input texture of the next pass. In the latter technique, the simulation is basically always a one pass simulation. This scheme of simulation improves significantly the quality of textures predicted. It has been found through previous works on Cu [13,27] that continuous simulation of the passes is successful only up to two passes, after which the deviations between experiment and simulation become significant. This could be attributed to the facts that: (i) after two passes the strain is very large (about shear of 4) where polycrystal models begin to fail and (ii) it is well known that there is a very significant grain refining process in ECAE, which is not modeled in the present simulations. In the present case, the validity of continuous simulation was not expected to be fully successful even up to two passes owing to the possibility of dynamic recrystallization of Al under the experimental conditions employed.

The grain refinement process due to continuous dynamic recrystallization changes the grain shape. Grain shape effects can be taken into account in the VPSC model. In the present modeling, it was approximated in the following way: at the beginning of the first pass, the grain shape was nearly equiaxed, so each grain was considered to be spherical and its shape development was allowed according to the imposed velocity field. At the end of the pass, a grain becomes very elongated. Knowing that in reality such a grain is already fragmented, we reset the grain shape of the grains to spherical at the beginning of each new pass. In this way, the shape evolution of a grain due to grain refinement could be taken into account in the polycrystal model, at least, in a first approximation.

4.1. Results of texture simulations

The results of texture simulations using the simple shear model in the VPSC polycrystal code with two families of slip systems following the three principal routes of ECAE deformation are displayed in Figs. 11–14. The one pass texture (Fig. 11) is common to all three routes and the textures predicted for the subsequent passes, namely routes A, B_c and C, are displayed in Figs. 12–14, respectively.

By comparing the textures predicted for the one pass deformed material (Fig. 11c) to the corresponding experimental texture (Fig. 11b), it can be said that the position of the components match the experimental texture, especially with regard to the rotated position of the cube texture. A particularity of the predicted texture is the existence of a fiber around the C_E orientation in the φ coordinate direction. This fiber joins the rotated cube components with C_E. This fiber is also well visible in the experimental texture, with the difference that its intensity is much less in the experiment. It looks continuous fiber only when lower intensity levels are also plotted. In general, the intensities of the experimental and predicted texture components are quite disproportionate; the predicted texture is stronger compared to the experimental texture.

Starting from pass two, the simulated textures are presented only in the 45° section of the ODF. For the positions of the ideal components of the textures in the ODF; see Fig. 5. After the second pass of route A (Fig. 12), the main characteristics of the textures are reproduced; there is significant deviation only in the A_{2E} component which is too strong in the simulation. This effect will be discussed in Section 5. The intensity of A_{2E} slightly decreases when the simulated texture is updated with the experimental texture of the first pass. In general, the intensity of the texture decreases with

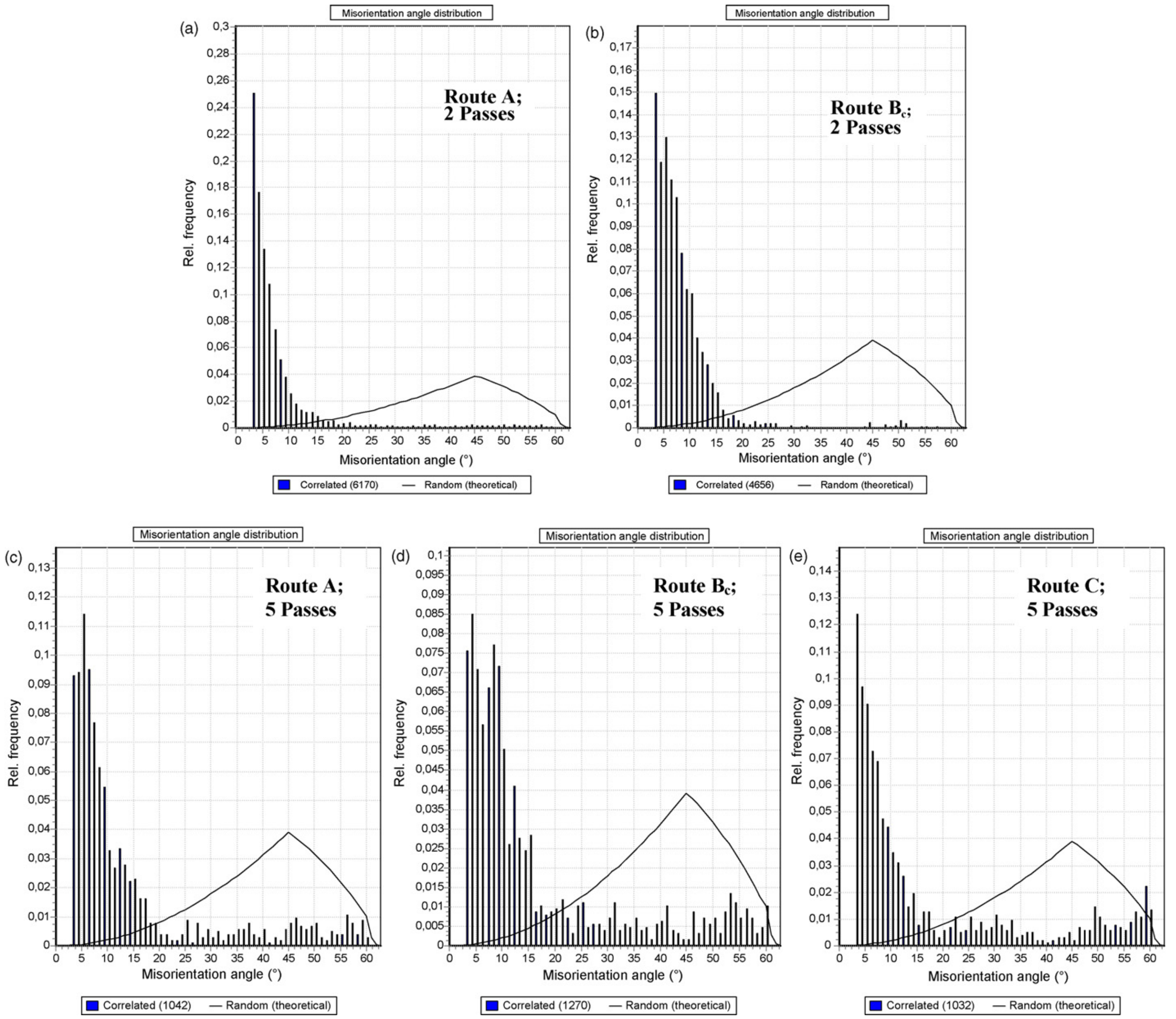

Fig. 10. The misorientation distribution plots for micrographs displayed in (a) route A after two passes, (b) route B_c after two passes, (c) route A after five passes, (d) route B_c after five passes and (e) route C after five passes.

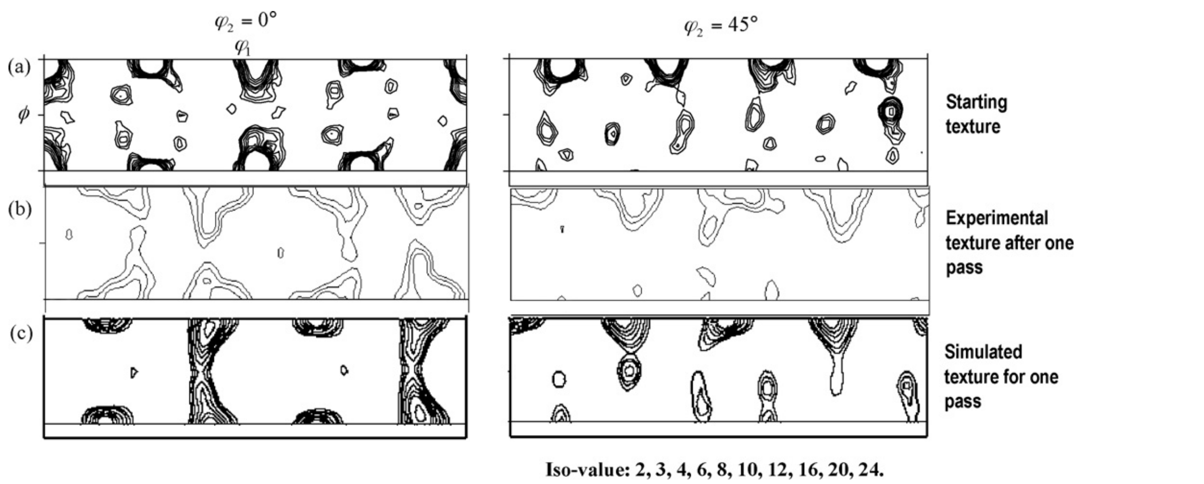

Fig. 11. The simulated texture for one pass deformed material presented along with the starting experimental texture and the experimental texture after one pass.

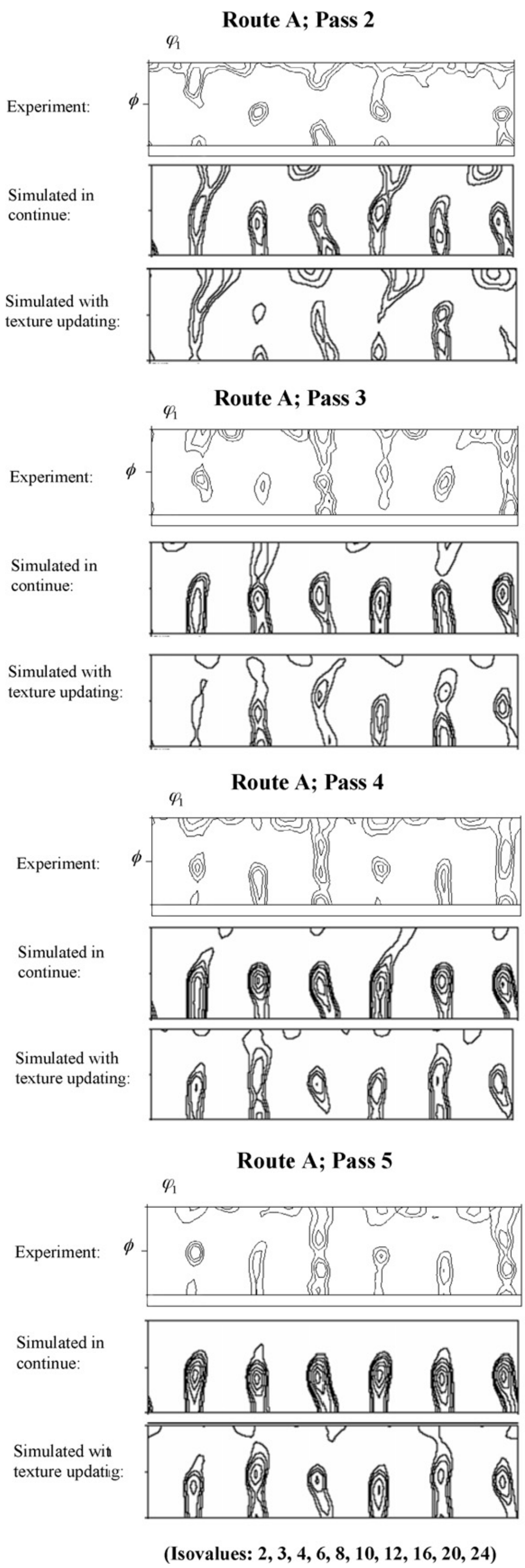

Fig. 12. Simulated textures in comparison with the experiment for route A in the $\phi_2 = 45^\circ$ section of the ODF.

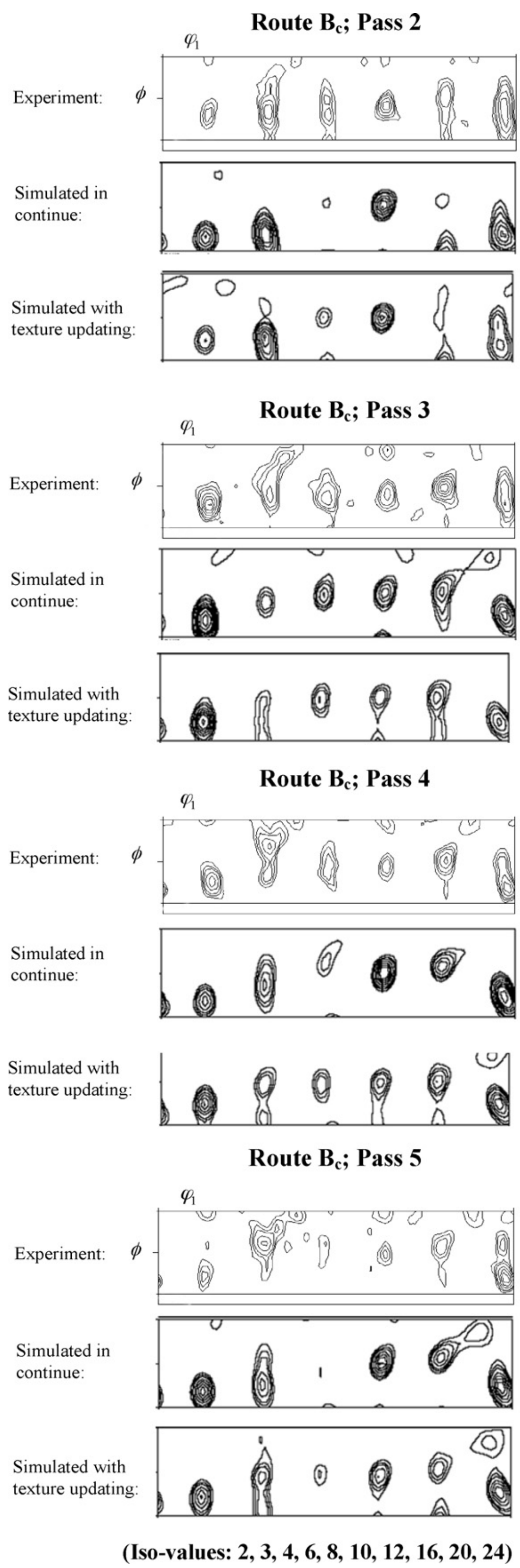

Fig. 13. Simulated textures for route B_c in the $\phi_2 = 45^\circ$ section of the ODF.

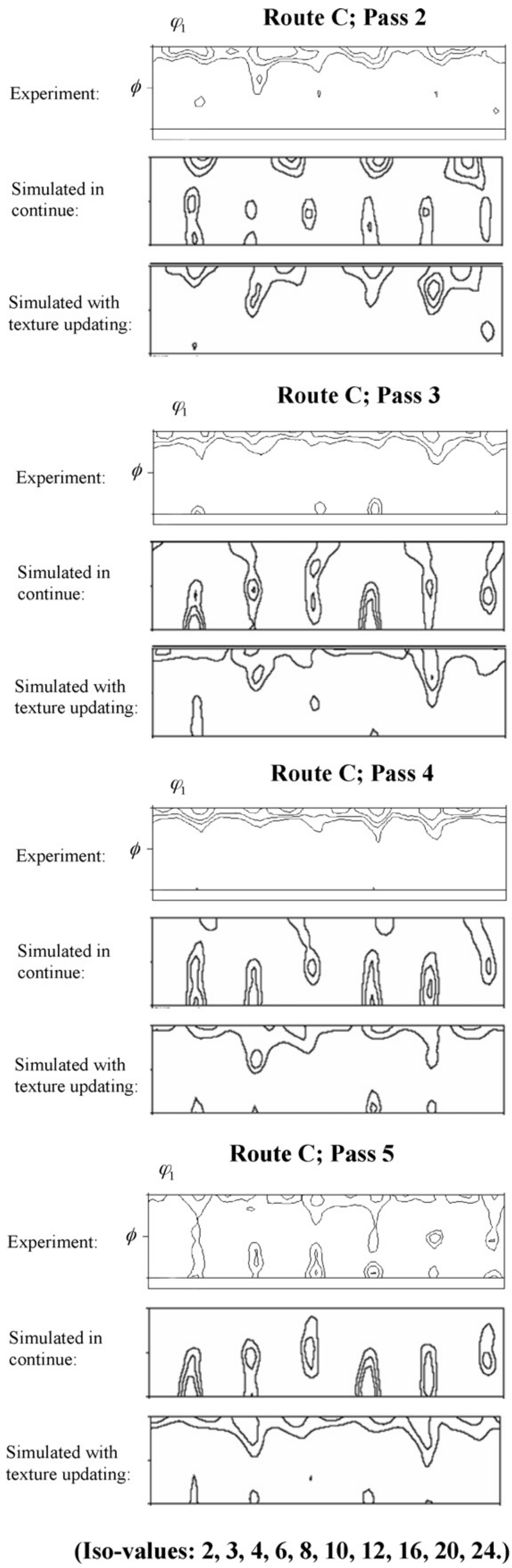

Fig. 14. Simulated textures for route C in the $\phi_2 = 45^\circ$ section of the ODF.

the texture updating simulation technique and approaches better the experimental texture. The simulation predicts both the B_E and $\bar{B}_E$ components while in the experiment, only B is strong. Similar observation is valid for the A and $\bar{A}$ components. Similar differences can be seen in the next passes, with the difference that $A/\bar{A}$ components both appear in the experimental and simulation textures. The rotated cube component, although present in the simulations, are not always predicted in the right position.

Much better agreements obtained for the route B_c textures (see Fig. 13). Generally, all components are reproduced in the right positions. The intensities of the textures also match the experiment, especially using in the texture updated predictions. Only the B_E' component, which becomes strong in the experiment at large number of passes, deviates from the simulations slightly. The rotated cube component is relatively weak, both in the experiments and the simulations.

Even better success has been reached in the route C pass simulations (see Fig. 14). This is quite unusual as route C was reported to be the most difficult to simulate [32]. However, the present route C textures are quite simple as they mostly consist in the rotated cube component. The deformation texture components are very weak or absent. They are only significant in the fifth pass texture. Again, the simulation results are very good with the texture updating technique while quite incorrect with the continuous simulations. In the latter, the rotated cube component progressively disappears at large number of passes while in the experiment, it is the strongest.

5. Discussion

5.1. Effect of processing route on texture formation

The pole figures and ODFs all show textures that have markedly different features as a function of processing route. The one pass texture being common to all routes, different textures appear in different routes. Within one route, however, the textures remain quite similar meaning that the texture stabilizes from pass two on. This is best seen in the pole figures in Fig. 4 where the entire texture is visible. One can see in the pole figures that route A and C textures are quite similar, however, the ODFs (Figs. 5 and 7) reveal important differences; they concern the shear deformation components that are quite significant in route A while nearly absent in route C (exemption is pass five). The common feature between these routes is the existence of the rotated cube fibers. They are readily visible both in the pole figures and the ODFs, and are especially strong in route C.

The route B_c texture is completely different from the textures in routes A and C. In this route the $B/\bar{B}$ components are strong and remain strong even in the fifth pass (see Fig. 6). This observation of a strong texture after five ECAE passes is in contradiction to some of the previous results on Al (99.5% pure) deformed by route B_c up to eight passes (with a 90° die angle) after which a random texture was reported [45]. However, the results in [45] were based on EBSD orientations measured in a small area of 6.6 μm × 10 μm. The presence of inhomogeneities in the microstructure of the material deformed by ECAE route B_c even at high strains have been reported by Gholinia et al. [8] and Mishin et al. [46]. It is possible, therefore, that the authors of [45] measured a local texture that is not representative of the overall texture. In our study, the area used for texture determination is 10 mm × 10 mm, which can be considered to represent the global texture. A very recent study by Cao et al. [47], who also studied commercially pure Al (99.5%) deformed by route B_c of ECAE, reveals that texture becomes stronger with number of ECAE passes. The explanation of this can be given on the basis of flow field of deformation. Since route B_c generates $B_E/\bar{B}_E$ components, which become cumulatively stronger according to the flow field description [13,27], the texture becomes stronger with number of passes. The evolution of B-type texture during route B_c, has also been reported by Terhune et al. [48].

The interpretation of the texture development in the different routes will be now discussed. As it has been shown earlier [49], the cube texture is not stable in shear deformation; it rotates with the shear-imposed rigid body rotation. The presence of the {1 0 0} non-octahedral slip system does not change this process. The exact cube would stay on the cube-fiber during this rotation; however, grains that deviate from the cube can rotate very far from the cube. This has been studied in cube oriented single crystal nickel [50]. The main orientation where the cube rotates is the A_{1E}. This is also observed in the present Al texture (see Fig. 11). This feature was also successfully simulated in [50]. At the same time, the cube component is retained, in a rotated position. In a subsequent pass, basically the same procedure is repeated and a nearly constant texture develops. Finally, all deformation texture components appear, however, with relatively low intensity (see Fig. 8).

In the route B_c processed materials, there is an out of plane rotation (90° rotation around the sample long axis) which brings the texture into a very different position with respect to the simpler A and B routes. This rotation changes the rotated cube position in such a way that it will not remain on the cube-fiber. Instead, it will rotate into positions that are not far from the $B_E/\bar{B}_E$ components into which the grains rotate. Route B_c reproduces the $B_E/\bar{B}_E$ components in each pass, this is why the texture intensity grows very high. Together with the $B_E/\bar{B}_E$ components, the B'_E component also develops and becomes strong. The formation of the B'_E component has not yet been explained in detail. This component – although near to the B fiber of shear textures – is not part of the B fiber.

In the route C processed materials, the shear direction changes in every pass into opposite which moves the cube only along the cube-fiber line. This is why the route C texture consists of mainly the rotated cube component.

5.2. Experiments vis-à-vis simulations

As presented in Section 4 above, the simulated textures are generally in good agreements with the measurements. Among the two techniques, it is the texture updating method that generally led to better results. (Note that in the first pass, the two techniques are identical.) Interestingly, the quality of the agreement depends on the route. It is very good in routes B_c and C and much less satisfactory in route A. One can speculate that the reason behind is the differences in the grain refinement processes in the experiments, which might be orientation dependent. They were not taken into account in the simulations. It is actually probable that the grain refinement is the most effective in route A. Another source of the differences could be statistical. Actually, the initial grain size being ~200 μm could be too large. When grain size is too big, deviations usually take place in the measured textures from the expected sample symmetries. In routes A and C, twofold symmetry is expected in the textures meaning a 180° rotation around the TD axis. This symmetry should make the B and $\bar{B}$ components equally strong (individually they are not centro-symmetric with respect to TD). They are, however, of very different intensities, especially in the pass two route A texture (see Fig. 12). Even if strong grain refinement is taking place, refined grains coming from the same 'parent' grain form some colonies because they remain not too far from each other in orientation space. This effect is quite visible in Fig. 9 where the microstructure is shown in EBSD images.

Another reason for the differences between simulations and experiments is the occurrence of continuous dynamic recrystallization. They are not taken into account in the simulations; at least, not directly. Actually, this effect is partially present in the texture updating simulations where the experimental texture is used in the subsequent pass. Nevertheless, during the pass, grain refinement is not modeled. Although significant efforts have been done in grain refinement modeling [51,52], an efficient grain refinement model is still missing in the literature. The differences with the experiments concern mostly the intensity of the texture components. The grain fragmentation process during ECAE not only leads to a very fine grain structure but also develop increasing misorientations across adjacent subgrains as a function of the number of ECAE passes. This process leads to increasing deviations between the modeled orientation of the grain and its real subgrain-orientation distribution. The first highly probable process that could lead to a change in the texture is dynamic restoration. In materials with high stacking fault energy like Al, dynamic recovery is highly probable. However, the possibility of dynamic recrystallization also cannot be ruled out; particularly owing to very high level of deformation per pass. The possible mechanism would be continuous dynamic recrystallization. The prior grains may develop an orientation gradient from the center of the grain to the edge, that is, the grain boundary. The misorientation at the center may be quite low, however, towards the grain boundary it may increase quite substantially leading to high angle boundaries, under the action of high stresses as applied during a deformation like ECAE.

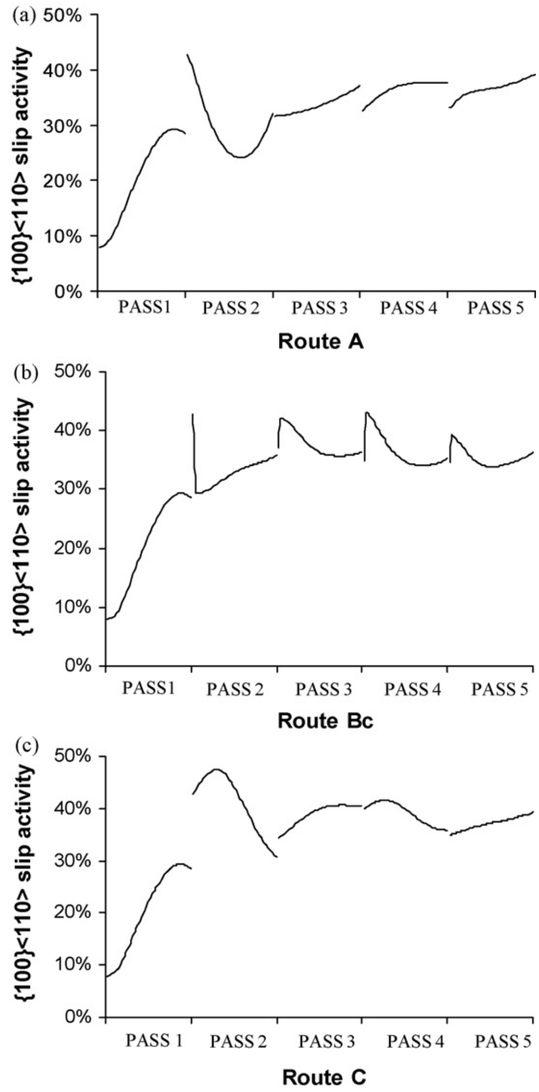

Fig. 15. Relative activity of the non-octahedral slip system family with respect to the total slip as obtained from texture modeling for routes A (a), B_c (b) and C (c) (obtained with the texture updating technique).

Finally, the role of non-octahedral slip in the texture development should be discussed. For this purpose, the slip activity in the {1 0 0} type non-octahedral slip family is plotted in Fig. 15. As can be seen, the {1 0 0} family becomes more and more active during ECAE. The initial 8% activity grows near to 30% in the first pass. During the first pass, the ratio of the strength of the {1 0 0} and {1 1 1} families was set to $r_{\tau c} = 1.5$. Starting from the second pass, they were set equal ($r_{\tau c} = 1$). As can be seen in Fig. 15, the activity of the non-octahedral slip family jumps to about 40% at the beginning of the second pass. This can be due to the lowering of the $r_{\tau c}$ value and can also be the effect of the strain path change between subsequent passes. Namely, for re-inserting the specimen into the die, it has to be turned 90° around the TD axis, which represents a 90° displacement of the whole texture in Euler space along the ϕ_1 coordinate. This means that the slip system selection is changing immediately as the second pass begins. Starting from the third pass, the slip activity of the non-octahedral slip shows nearly the same variation in each pass which is another sign of the stabilization of a cyclic-texture development.

The non-octahedral slip remains at a high level in all passes and all routes; at about ∼35%. Its contribution is primordial in the evolution of the texture. Without introducing this slip system family, the simulated textures are in bad agreement with the experiments. A more sophisticated hardening law should be developed for the purpose of a better control between the activities of the two competing slip system families.

6. Conclusions

1. The textures that develop in ECAE of CP Al consisting of an initially strong cube texture depend strongly on the ECAE route. In route A and C, the cube component appears in rotated positions forming a non-even intensity cube-fiber with fiber axis being the TD. In route C, only the cube-fiber is present, while in route A, the shear deformation texture components also develop. In route B_c, the cube-fiber is non-existing and strong B and $\bar{B}$ components appear. Another component, the B'_E has also been observed in route B_c textures which is not far from the B fiber.
2. Continuous dynamic recrystallization is taking place at room temperature in CP Al due to the large strains applied in ECAE testing. This produces a fine grained structure with slightly elongated grains.
3. Texture simulations following the simple shear with the VPSC model reproduced the main elements of the texture development in each routes up to five passes. In this modeling, in addition to the usual {1 1 1}⟨1 1 0⟩ slip of fcc materials, the {1 0 0}⟨1 1 0⟩ non-octahedral slip is also an important slip process, which makes about ∼35% of the imposed deformation.

References

[1] V.M. Segal, Materials Science and Engineering A 197 (1995) 157–164.
[2] V.M. Segal, Materials Science and Engineering A 271 (1999) 322–333.
[3] A. Gholinia, P.B. Prangnell, M.V. Markushev, Acta Materialia 48 (2000) 1115–1130.
[4] C. Pithan, T. Hashimoto, M. Kawazoe, J. Nagahora, K. Higashi, Materials Science and Engineering A 280 (2000) 62–68.
[5] P.L. Sun, P.W. Kao, C.P. Chang, Materials Science and Engineering A 283 (2000) 82–85.
[6] U. Chakkingal, P.F Thomson, Journal of Materials Processing Technology 117 (2001) 169–177.
[7] W.H. Huang, L. Chang, P.W. Kao, C.P. Chang, Materials Science and Engineering A 307 (2001) 113–118.
[8] A. Gholinia, P. Bate, P.B. Prangnell, Acta Materialia 50 (2002) 2121–2136.
[9] J.R. Bowen, O.V. Mishin, P.B. Prangnell, D. Juul Jensen, Scripta Materialia 47 (2002) 289–294.
[10] L. Dupuy, E.F. Rauch, Materials Science and Engineering A 337 (2002) 241–247.
[11] S.C. Baik, Y. Estrin, H.-S. Kim, R.J. Hellmig, Materials Science and Engineering A 351 (2003) 86–92.
[12] S. Suwas, L.S. Tóth, J.J. Fundenburger, A. Eberhardt, W. Skrotzki, Scripta Materialia 49 (2003) 1203–1208.
[13] L.S. Tóth, R. Arruffat Massion, L. Germain, S.C. Baik, S. Suwas, Acta Materialia 52 (2004) 1885–1898.
[14] S. Suwas, A. Eberhardt, L.S. Tóth, J.J. Fundenberger, T. Grosdidier, Proceedings of Second International Conference on Recrystallisation and Grain growth, Trans Tech Publications Inc., Switzerland, 2004, pp. 1325–1330.
[15] C.Y. Yu, P.L. Sun, P.W. Kao, C.P. Chang, Materials Science and Engineering A 366 (2004) 310–331.
[16] M.V. Markushev, M.Yu. Murashkin, Materials Science and Engineering A 367 (2004) 234–242.
[17] S. Ferrasse, V.M. Segal, F. Alford, Materials Science and Engineering A 372 (2004) 44–55.
[18] S. Li, I.J. Beyerlein, C.T. Necker, D.J. Alexander, M. Bourke, Acta Materialia 52 (2004) 4859–4875.
[19] S. Suwas, L.S. Toth, J.-J. Fundenberger, A. Eberhardt, Solid State Phenomena 105 (2005) 357–362.
[20] S. Li, I.J. Beyerlein, D.J. Alexander, S.C. Vogel, Acta Materialia 53 (2005) 2111–2125.
[21] S. Suwas, L.S. Toth, J.-J. Fundenberger, T. Grosdidier, W. Skrotzki, Solid State Phenomena 105 (2005) 345–350.
[22] R. Arruffat-Massion, S. Suwas, L.S. Tóth, W. Skrotzki, J.-J. Fundenberger, A. Eberhardt, Materials Science Forum 495–497 (2005) 839–844.
[23] P.J. Apps, M. Berta, P.B. Prangnell, Acta Materialia 53 (2005) 499–511.
[24] J. Mao, S.B. Kang, J.O. Park, Journal of Materials Processing Technology 159 (2005) 314–320.
[25] M. Cabibbo, E. Evangelista, C. Scalabroni, Micron 36 (2005) 401–414.
[26] A. Mishra, V. Richard, F. Grégori, R.J. Asaro, M.A. Meyers, Materials Science and Engineering A 410–411 (2005) 290–298.
[27] S. Suwas, L.S. Tóth, J.J. Fundenberger, A. Eberhardt, W. Skrotzki, Metallurgical and Materials Transactions A 37A (2006) 739–753.
[28] W. Skrotzki, N. Scheerbaum, C.-G. Oertel, H.-G. Brokmeier, S. Suwas, L.S. Tóth, Materials Science Forum 503–504 (2006) 99–106.
[29] W. Skrotzki, N. Scheerbaum, C.-G. Oertel, H.-G. Brokmeier, S. Suwas, L.S. Tóth, Acta Materialia 55 (2007) 2211–2218.
[30] W. Skrotzki, N. Scheerbaum, C.-G. Oertel, R. Arruffat-Massion, S. Suwas, L.S. Tóth, Acta Materialia 55 (2007) 2013–2024.
[31] I.J. Beyerlin, L.S. Tóth, C.N. Tome, S. Suwas, Philosophical Magazine 87 (2007) 885–906.
[32] I.J. Beyerlin, L.S. Tóth, Progress in Materials Science 54 (2009) 427–510.
[33] P. Van Houtte, ODF MTM−−FHM Software, Version, 2000.
[34] H.-J. Bunge, Zeitschrift Fur Metallkunde 56 (1965) 872.
[35] A. Molinari, L.S. Tóth, Acta Metallurgica et Materialia 42 (1994) 2453–2458.
[36] B. Bacroix, J.J. Jonas, Textures and Microstructures 8&9 (1988) 267–311.
[37] C. Maurice, J.H. Driver, Aluminium Alloys 217 (1996) 547–552.
[38] C. Maurice, J.H. Driver, Acta Materialia 45 (1997) 4639–4649.
[39] F. Perocheau, J.H. Driver, T. Aukrust, Texture and Anisotropy of Polycrystals 273-2 (1998) 377–382.
[40] F. Perocheau, J.H. Driver, International Journal of Plasticity 16 (2000) 73–89.
[41] J. Driver, F. Perocheau, C. Maurice, Aluminium Alloys 331-3 (2000) 43–56.
[42] F. Perocheau, J.H. Driver, International Journal of Plasticity 18 (2002) 185–202.
[43] W. Robert, D. Piot, F. Eberl, J.H. Driver, Aluminium alloys 2002: Their Physical and Mechanical Properties, Pts 1-3, Materials Science Forum 396-4 (2002) 365–370.
[44] M. Crumbach, G. Gottstein, L. Lochte, D. Piot, J. Driver, C.M. Allen, J.F. Savoie, Aluminium alloys 2002: Their Physical and Mechanical Properties, Pts 1-3, Materials Science Forum 396-4 (2002) 357–364.
[45] P.L. Sun, P.W. Kao, C.P. Chang, Materials Science and Engineering A283 (2000) 82–85.
[46] O.V. Mishin, D. Juul Jensen, N. Hansen, Materials Science and Engineering A 342 (February (1–2)) (2003) 320–328.
[47] W.Q. Cao, A. Godfrey, Q. Liu, Materials Science and Engineering A 361 (November (1–2)) (2003) 9–14.
[48] S.D. Terhune, D.L. Swisher, K. Oh-Ishi, Z. Horita, T.G. Langdon, T.R. McNelley, Metallurgical and Materials Transactions A 33A (2002) 2173–2184.
[49] L.S. Tóth, J.J. Jonas, Textures and Microstructures 10 (1989) 195–209.
[50] W. Skrotzki, L.S. Tóth, B. Klöden, H.-G. Brokmeier, R. Arruffat-Massion, Acta Materialia 56 (2008) 3439–3449.
[51] I.J. Beyerlein, R.A. Lebensohn, C.N. Tome, Materials Science and Engineering A345 (2003) 122–138.
[52] A.A. Nazarov, N.A. Enikeev, A.E. Romanov, T.S. Orlova, I.V. Alexandrov, I.J. Beyerlein, R.Z. Valiev, Acta Materialia 54 (2006) 985–995.